 doi:10.20944/preprints202204.0171.v1

Mechanically Enhanced Hydrophobic Metal Surfaces Enabled by 3D Gradient Structures

Xiaohan Zhang [a], Jian Liu [a], Min Xia [c], Yaowu Hu [a,b,*]

[a]The Institute of Technological Sciences, Wuhan University, Wuhan, 430072, China
[b]School of Power and Mechanical Engineering, Wuhan University, Wuhan, 430072, China
[c]Department of Engineering, Lancaster University, Lancaster, LA1 4YW, United Kingdom
*Corresponding author: Yaowu Hu
E-mail: yaowuhu@whu.edu.cn

Abstract

The mechanical properties and stability of hydrophobic surface structures prepared by traditional methods are still the main technical bottlenecks restricting the broad application of hydrophobic systems on workpiece surfaces. In this contribution, we propose a technique called selective laser shock peening (SLSP) to enable large-scale high efficient, low-cost manufacturing of hydrophobic metal surfaces with enhanced mechanical properties for durable applications. Using the method of experimental investigation combined with numerical calculation, the hydrophobic properties, mechanical properties, and tribological properties of the samples prepared under SLSP, all-laser shock peening (ALSP), and non-laser shock peening (NLSP) are studied. The SLSP process could prepare a 3D gradient structure material with surface structures, a two-phase (strong phase, soft phase) distribution on the surface, and a multi-level gradient distribution in the thickness direction. Compared with the 2D gradient structure prepared by the traditional process, 3D gradient structures by SLSP have more significant advantages in improving the wetting behavior and the mechanical properties of the material, which proves SLSP to be a novel method to fabricate functional metal surface structures, with highly high engineering application value.

Keywords: Selective laser shock peening; Hydrophobic properties; Mechanical properties; 3D gradient structure

1. Introduction

The hydrophobicity of a material's surface is of significant importance for realizing anti-icing, anti-fouling, self-cleaning and corrosion-prohibitive applications and thus determines the material's service life [1]. Researchers have used different process methods to effectively control the hydrophobic properties of the metal surface by adjusting the microscopic morphology and chemical composition of the metal surface[2–4]. However, the main technical bottlenecks restricting large-scale applications of existing hydrophobic structuring methodologies are the fragility of the fabricated hydrophobic structures and the lack of flexibility of the processing technology for 3D surfaces with various compositions[5–7]. Under complex multi-physical external environmental loads, such as cyclic mechanical loading, chemical corrosion, and abrasion, the reliability of the hydrophobic structure is reduced very quickly. The performances in these situations are thus highly related to defect evolution and the mechanical properties of the surface and sub-surface.

Preprints (www.preprints.org) | NOT PEER-REVIEWED | Posted: 18 April 2022 doi:10.20944/preprints202204.0171.v1

Laser surface structuring is believed to be an enabling technology for hydrophobic surfaces fabrication[8–10]. Femtosecond laser direct ablation of the target material to generate various nanoscale features has drawn intense attention in the past decades[11,12]. However, femtosecond lasers have different delicate optics, making the process expensive and less efficient for large-scale applications. Pulsed laser shock imprinting can generate sub-10 nanometer geometries but suffers from the thickness limitations of the sample[13–15]. Direct nanosecond laser ablation can increase efficiency and lower the fabrication cost [16]. However, the treated surfaces become brittle and are relatively flat, resulting in uncomplicated fracture of the functional nanostructures and less energy absorption under impact loading[17]. A partially random shot peening technique is proposed to balance the relationship between strength and ductility but can only fabricate microscale randomly distributed surface dents[18,19]. Controllability of surface changes is difficult to achieve. A mechanically robust hydrophobic design based on microscale armor and nanoscale hydrophobic structures is introduced to alleviate the exclusiveness of mechanical robustness and water repellence[4]. However, for large-scale industrial applications, it is not yet feasible to fabricate such armors on the targeted surfaces without degrading the integrity of the character, in addition to economic and efficiency reasons.

In this paper, we propose a realistic and straightforward strategy to fabricate self-armored multiscale hydrophobic surfaces in a flexible and large-scale fashion. The application scope of the laser shock wave is expanded, and new technology of selective laser shock preparation of high-reliability hydrophobic surface structure is proposed by combining the two process methods of laser shock peening and forming. The hydrophobic, mechanical, and tribological properties of pure copper were studied under three different process conditions: SLSP, ALSP, and NLSP. The numerical simulation results of the finite element and molecular dynamics provide theoretical support for the experimental data. The application of this technology can achieve both excellent hydrophobic properties and mechanical properties of metallic components, which opens avenues for high-performance and durable engineering applications.

2. Experimental

2.1. Material details

A copper plate with a purity of 99.99% was selected for selective laser strengthening treatment. The thickness of the pure copper plate was 200 μm, and its main element composition is shown in **Table 1**. After polishing it to the mirror surface with 1500 mesh sandpaper, a tube furnace was used for pre-annealing. The annealing atmosphere was high-purity nitrogen; the annealing temperature was 600 ℃; the holding time was 1 h, and the heating rate was 5 ℃/min. As shown in **Fig.S1**, 316 stainless steel metal woven thin meshes of three different sizes were used as auxiliary structural members of the SLSP, acting as optical masks and momentum transmission layers. The mesh size of the thin metallic mesh (a*b) and the thickness (d) of the thin metallic mesh are shown in **Table 2**.

Table 1 Main element composition of copper plate

Element	Bi	As	Sb	Fe	Pb	S	Cu
Content(*wt*%)	0.0008	0.0013	0.0015	0.0036	0.0038	0.0044	99.99

Preprints (www.preprints.org) | NOT PEER-REVIEWED | Posted: 18 April 2022 doi:10.20944/preprints202204.0171.v1

Table 2 mesh size and the thickness of the thin metallic mesh

Serial number	a×b (μm²)	d (μm)
Case 1	100×100	50
Case 2	150×225	70
Case 3	250×425	80

2.2. SLSP process

Fig.1 showed the schematic diagram of the process of SLSP. The nanosecond pulsed laser was used for SLSP, and the process parameters are shown in **Table 3**. A pure copper plate with a thin metallic mesh on the surface was placed in the center of the liquid pool. In the liquid pool, the distance between the liquid level of deionized water and the surface of the pure copper plate was 5 mm. The pulsed laser acted on the surface of the thin metallic mesh or pure copper plate through the reflector, focusing mirror, and protective mirror. The focusing mirror adopted a convex optical lens with a focal length of 175 mm; the reflecting mirror adopted an optical total reflection plane mirror with 1064 nm. The protective mirror was used to prevent splashes of liquid droplets from contaminating the mirror group. The airflow generated by the air blowing device was used to change the direction of droplets splashing and prevent the droplets from depositing on the surface of the mirror group and affecting the beam quality. The three-coordinate mobile platform was used to change the position where the laser interacted with the sample.

Table 3 SLSP process parameters for copper metal

Process parameters	value
Laser wavelength	1064 nm
Laser pulse width	7 ns
Laser pulse frequency	10 Hz
Laser current	10 A
Laser voltage	900 V
Overlap rate of the laser spot	50%
Constraint layer material	Deionized water
Constraint layer thickness	5 mm

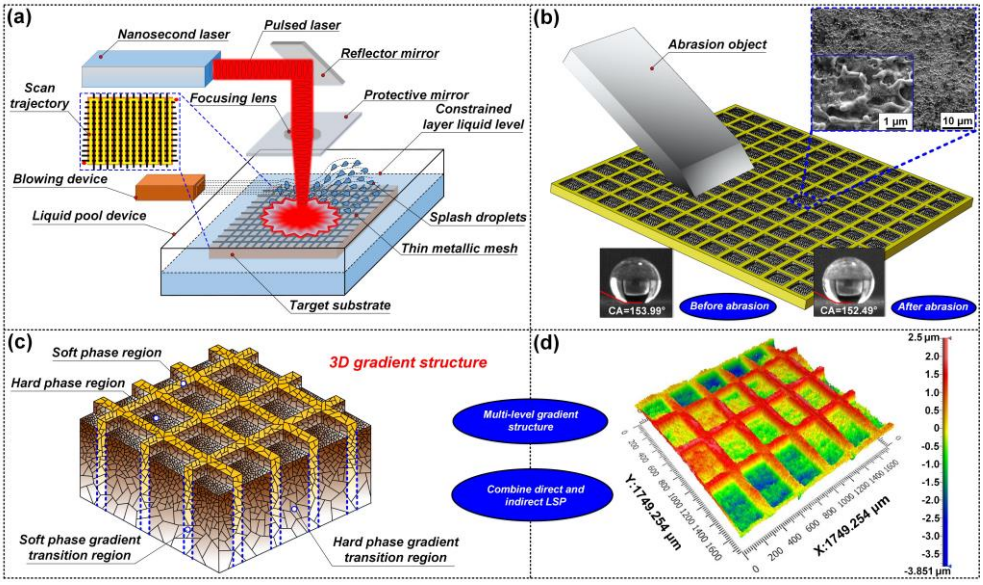

Fig.1. Schematic diagram of the process of SLSP

Preprints (www.preprints.org) | NOT PEER-REVIEWED | Posted: 18 April 2022 doi:10.20944/preprints202204.0171.v1

((a) Schematic diagram of the SLSP process equipment; (b) Self-armored multiscale hydrophobic surfaces; (c) Novel 3D gradient structure; (d) 3D profile of the sample prepared by SLSP)

2.3. Experimental equipment and characterization methods

The metallographic microscope (BX53M, Olympus Inc., Japan) was used to observe the macroscopic appearance of the sample after laser shock. Sandpaper (240-3000 mesh) and diamond polishing compound (W1.5-0.5) were used to grind and polish the samples. Aqua regia (a 3:1 mixture of concentrated hydrochloric acid and concentrated nitric acid by volume) was used to etch the samples. The field emission scanning electron microscope (MIRA 3, TESCAN Brno,s.r.o. Inc., Czech Republic) with an energy dispersive spectrometer (Aztec Energy, Oxford Instruments Nanoanalysis Inc., U.K.) was used to observe the microscopic morphology and element content of the sample after laser shock. The surface topography and roughness were measured using the white light interferometric 3D profiler (NewViewTM 9000, ZYGO Inc., U.S.A.). The goniometry instrument (JCY-4, Fangrui Inc., China) was used to measure the contact angle of the sample at room temperature (25± 2 ℃) with a 4 μL distilled water droplet. The 240-mesh sandpaper was placed on the surface of the samples. Then the samples were subjected to mechanical friction treatment with the help of a weight of 500 g. Then, utilizing the goniometry instrument, the hydrophobic angle of the surface of the sample after the friction treatment was continued to be tested. The nanoindenter (TI 950 TriboIndenter™, Bruker Inc., U.S.A.) was used to test the hardness distribution of the sample. The pressure load was 3000 μN, the loading method was 5 s loading, 2 s holding the load, and 5 s unloading. XRD (X' Pert PRO, Almelo, Netherlands) was performed to investigate coupon phase structure and crystal orientation before and after SLSP. The scan was performed using Cu Kα1 radiation (λ=0.1541 nm) at the 2θ range from 20°to 80°at the rate of 4 ° per minute and a counting time of 1 s per step. The integrated patterns were then analyzed using Jade 6 for phase identification. The universal testing machine (5956, Instron Inc., U.S.A.) was used to test the tensile properties of the specimen, and the tensile rate was 2 mm/min. The micro-structures in the thickness direction of the cross-section of the sample prepared by SLSP were characterized via T.E.M. (JEM-2100F, JEOL Inc., Japan) operated at an accelerating voltage of 200 kV. With the aid of a friction and wear testing machine (M-2000, Henxu Inc., China), and using 316L stainless steel dual balls with a diameter of 6 mm, dry sliding friction and wear experiments at room temperature were carried out. After laser shock treatment, the samples were cleaned with acetone and an ultrasonic cleaner. After cleaning, the sample was immersed in an ethanol solution containing 1.5% volume percent of chlorosilane reagent [CF3(CF2)5(CH2)2SiCl3] for 3 h 30 min at room temperature. The samples were then rinsed with deionized water and dried with compressed air. Finally, the samples were dried using a vacuum oven with a temperature of 80 ℃ and a holding time of 1 h.

2.4. Finite Element Simulation and Molecular Dynamics Numerical Calculation

Finite Element (F.E.) simulation: The ABAQUS finite element simulation software was used to calculate the numerical magnitude and distribution of residual stress of the specimen prepared by SLSP. In this paper, ABAQUS/Explicit module was used to solve the dynamic transmission process of the shock wave until the end of plastic deformation. Then, the deformation and stress-strain state translated by ABAQUS/Explicit was imported into the ABAQUS/Standard module for further solution. The stress and strain were fully released, and the quasi-static process was reached. In addition, with the help of ABAQUS simulation software, based on the ductile

Preprints (www.preprints.org) | NOT PEER-REVIEWED | Posted: 18 April 2022 doi:10.20944/preprints202204.0171.v1

damage model, a uniaxial tensile numerical model of the samples prepared by selective laser shock peening was established to evaluate the tensile properties of the prepared samples under different processing.

Furthermore, we verified the nanoscale plasticity mechanism of Cu by molecular dynamics (M.D.) simulation method using a large-scale atomic/molecular massively parallel simulator (LAMMPS[20]. A Cu model with a dimension of 40.2 nm×20.1 nm×10.1 nm was established. And the periodic boundary was used in *x*, *y*, *and z* directions. The embedded-atom method (E.A.M.) potential was selected to describe Cu atoms' interaction [21]. The structural optimization was performed using the conjugate gradient (C.G.) algorithm to minimize. Subsequently, the model was relaxed for 50 ps under the N.P.T. ensemble. The strain rate for uniaxial compression was set to 10E9 s^{-1}. Visualization of atoms and analysis of dislocations was achieved using OVITO[22].

3. Results and discussion

3.1. Analysis of surface and cross-sectional topography

Fig.2 shows the surface structure of the samples prepared by SLSP. Array-like ablation morphologies were fabricated on the surface of metal substrates by SLSP. The ablated areas appeared dark black, and the non-ablated regions seemed to be bright yellow. The ablation morphology presented on the surface of the substrate was quasi-rectangular, which corresponds to the shape of the mesh of the thin metallic mesh, and was equivalent to the size of the mesh of the thin metallic mesh. The direct irradiation of pulsed laser on the copper surface would induce high-temperature plasma, which would cause ablation. At the same time, the thin metallic mesh acts as a protective layer so that the surface of the copper material covered by the thin metallic mesh would not appear ablated. Finally, the surface of the samples prepared by SLSP showed a prominent array of ablation morphology. By observing the Sub-Fig (c) for the thin metallic mesh with a larger mesh size, the surface of the substrate presented strip-shaped indentations due to the concentration of stress. In fact, under the coverage of thin metallic mesh of different sizes, the actual interaction area of laser and copper material was separate. By selecting the same surface area and counting the area fraction occupied by the ablated area, it was found that: In case 1, the area fraction of the ablated area was the smallest, which was 40.7%; In case 2, the area fraction of the ablated area was next, which was 46.1%; In case 3, the area fraction of the ablated area was the largest, which was 54.7%. The Sub-Fig (d) was the SEM photograph corresponding to the Sub-Fig (c). The laser shock peening area was relatively rough. In contrast, the non-laser shock peening area was relatively smooth, and the two regions showed noticeable contrast differences. The Sub-Fig (e) was a partially enlarged SEM photograph corresponding to the yellow box marked A in Sub-Fig (d). The Sub-Fig (e) showed a transition between the laser shock peening and non-laser shock peening areas. The Sub-Fig (f) was a partially enlarged SEM photograph corresponding to the yellow box marked B in Sub-Fig (d). Observing Sub-Fig (f), it was found that there were many water ripple structures in the laser shock peening area.

Preprints (www.preprints.org) | NOT PEER-REVIEWED | Posted: 18 April 2022 doi:10.20944/preprints202204.0171.v1

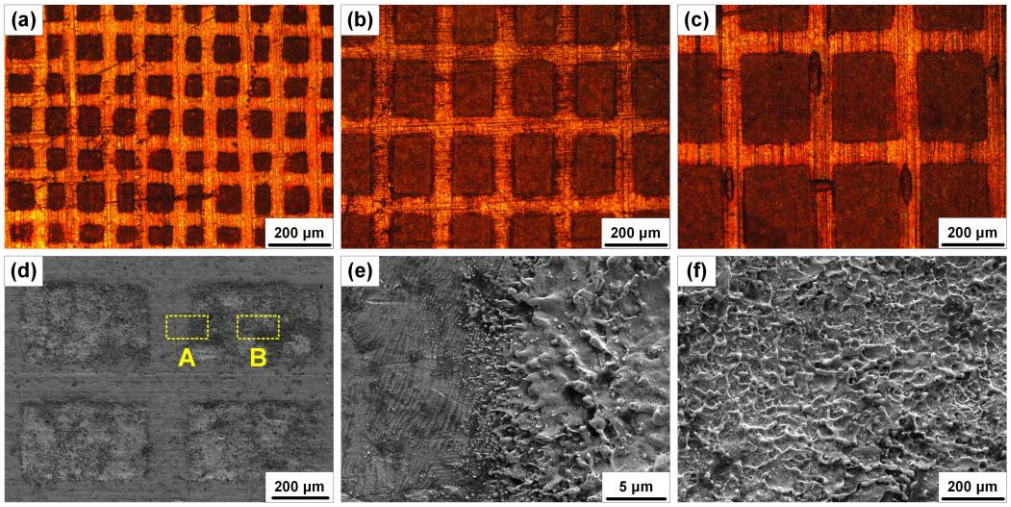

Fig.2. OM and SEM images of the surface of the samples prepared by SLSP ((a) OM picture/SLSP/case 1; (b) OM picture/SLSP/case 2; (c) OM picture/SLSP/case 3; (d) SEM picture of the surface of case 3; (e) Partially enlarged SEM photograph corresponding to the yellow box marked A in Sub-Fig (d); (f) Partially enlarged SEM photograph corresponding to the yellow box marked B in Sub-Fig (d))

The good hydrophobicity of the sample surface prepared by SLSP was primarily due to the unique microstructure of the sample surface. During the SLSP operation, the thin metal mesh first acted as an optical mask and a stress wave transmission layer. Part of the pulsed laser beam interacted directly with the copper material's surface through the thin metallic mesh. In contrast, the other part of the pulsed laser beam interacted with the thin metallic mesh. After the pulsed laser interacted directly with the copper surface, the material surface exhibited the typical "crater"-like micro-nano ablation morphology shown in **Fig.S2**, caused by laser-induced plume aggregation and redeposition[23]**.** However, due to the covering of the thin metal mesh, the material under the metal mesh avoided the direct interaction with the plume, which produced an alternately regular array ablation morphology on the surface of the material.

Fig.3 shows the 3D profiles of the samples under different processing conditions. The roughness of the sample surface could be indirectly reflected by comparing the mean arithmetic height (Sa) of the samples prepared under different processing conditions. Compared with the NLSP sample, the roughness of the laser shock treated sample was significantly increased, and the arithmetic means two orders of magnitude improved height (Sa). The roughness of the SLSP sample was greater than that of the ALSP sample. The roughness of the SLSP/case1 sample was similar to that of ALSP. However, with the increase in the mesh size of the thin metallic mesh, the roughness of the samples gradually increased. The surface of the samples prepared by the SLSP process showed an apparent array of groove morphology, and the groove size increased with the increase of the mesh size of the thin metallic mesh. Compared with the area covered by the thin metallic mesh, the material's surface below the mesh area had noticeable depressions. During the SLSP operation, the thin metallic mesh in the area covered with the thin metallic mesh and the copper surface without the thin metallic mesh interacted with the laser simultaneously. When the laser interacts with the material, it induces a plasma and generates a stress shock wave. Under the confinement of the confinement layer on the material's surface, the stress wave propagated along the direction of the material thickness. In the one-dimensional strain state, when the peak pressure

Preprints (www.preprints.org) | NOT PEER-REVIEWED | Posted: 18 April 2022 doi:10.20944/preprints202204.0171.v1

of the stress wave exceeded the Hugoniot elastic limit of the material, the surface layer of the material tended to deform in the local range of the laser spot. Due to the constraints of the surrounding material, high-amplitude residual compressive stress would be generated on the surface of the material. The residual compressive stress existing on the surface destroyed the equilibrium state of the internal force system of the material. A new force system was generated inside the material to balance the induced residual compressive stress, forming an uneven stress distribution in the thickness direction of the material. This non-uniform stress distribution in the thickness direction led to plastic deformation of the material. The stress wave would decay in the process of downward propagation, and the surface of the material directly interacting with the laser would produce obvious plastic deformation. However, the peak pressure of the stress wave propagating to the material's surface after passing through the thin metallic mesh was minimal, which could not produce effective plastic deformation. **Fig.S3** showed the 2D profiles of the samples under different processing conditions. The extraction path of each curve in **Fig.S3** is the corresponding black dotted line in each Sub-Fig in **Fig.3**. **Fig.S3** could more quantitatively reflect the roughness of the sample surface under different processing conditions. Combined with **Fig.3** and **Fig.S3**, the volume of pits on the sample's surface under different selective laser shock conditions could be roughly estimated. The pits produced by laser shock are approximately regarded as regular cuboids. Combined with Table 2 and Figure 4, the volume of the micro pits formed on the sample's surface under different thin metallic mesh sizes was calculated. The calculation results showed that the average groove volume of the sample surface corresponding to SLSP/case1 was about 21000 μm^3; the average groove volume of the sample surface corresponding to SLSP/case2 was about 64000 μm^3; the average groove volume of the sample surface corresponding to SLSP/case3 was about 320000 μm^3(Sub-Fig (d)).

The plasma expansion induced by the laser's interaction with the material created a pressure shock wave. The pressure wave propagated along with the thickness of the material and gradually decayed. When the impact pressure generated by the stress wave exceeded the yield strength of the material, the material itself would produce irreversible plastic deformation. Compared with the direct interaction between the pulsed laser and copper, when the pulsed laser interacted with the thin metal mesh through the confinement layer, the metal mesh itself acted as a sacrificial layer to excite pressure shock waves. The shock wave was gradually attenuated by propagating downward along the mesh body, resulting in a decrease in the intensity of the pressure wave indirectly acting on the copper surface. Compared with the copper surface in the area covered by the thin metal mesh, the copper surface outside the area covered by the thin metal mesh was recessed inward, resulting in more severe plastic deformation. The surface structure of the sample was closely related to its hydrophobic performance. This paper explored the relationship between surface structure and hydrophobic performance in the summary of 3.2.

Preprints (www.preprints.org) | NOT PEER-REVIEWED | Posted: 18 April 2022 doi:10.20944/preprints202204.0171.v1

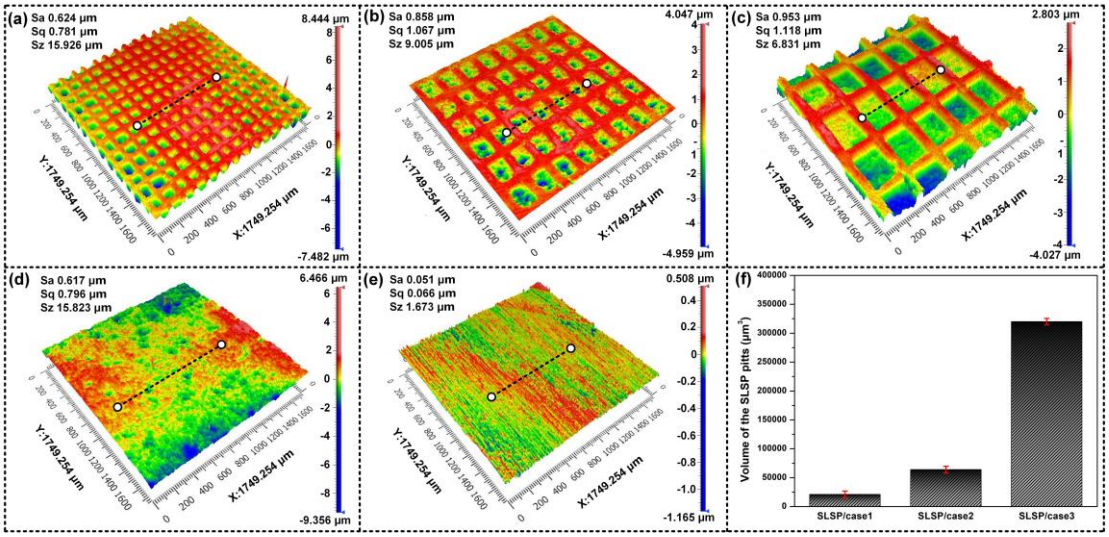

Fig.3. 3D profiles of the samples under different processing conditions
((a) SLSP/case 1; (b) SLSP/case 2;(c) SLSP/case 3;(d) ALSP;(e) NLSP; (f) Volume of the pitts)

Fig.4 shows the grain topography of the cross-section of the SLSP-prepared samples. After the pulsed laser interacted directly or indirectly with the material, different degrees of grain refinement would occur in the thickness direction of the material. The grain size of the material surface region was smaller than that of the material bottom layer region. It was worth noting that the grain refinement of the area without mesh directly interacting with the pulsed laser was greater than that of the area covered by the thin metallic mesh, and the depth of the refined layer was about 100 μm. Sub-Fig (b) showed the 3D profile of the micro pits prepared by SLSP. After the SLSP process, the surface of the material in the area directly affected by the laser underwent severe plastic deformation, forming a pit morphology. Sub-Fig (c) was the length of the boundary from point A to point B in Sub-Fig (b). The vertical distance from the bottom of the pit to the sample surface was about 20 μm. The laser shock could cause obvious plastic deformation of the material and form the microstructure of the grain size gradient surface in the thickness direction, which undoubtedly provided conditions for the adequate preparation of high-reliability hydrophobic surface structures.

Preprints (www.preprints.org) | NOT PEER-REVIEWED | Posted: 18 April 2022 doi:10.20944/preprints202204.0171.v1

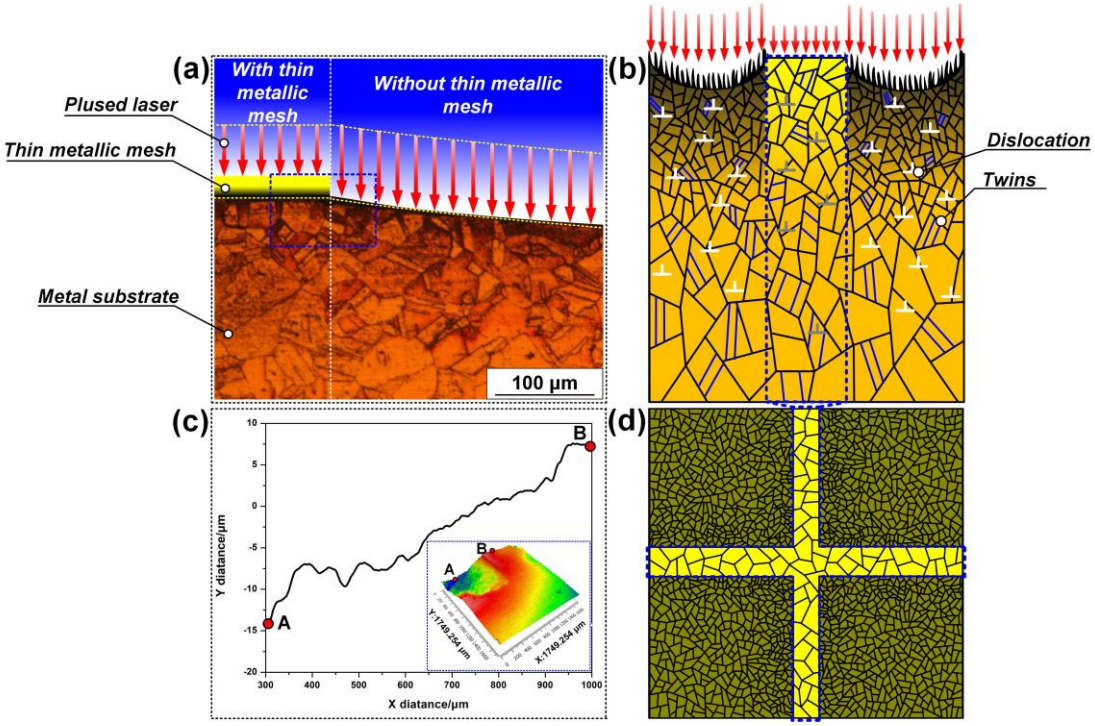

Fig.4. Grain topography of the cross-section of the SLSP-prepared samples ((a) OM image of the cross-section of the SLSP sample; (b) Schematic diagram of grain size transition in cross-section of the SLSP sample; (c) 3D profile of the sample in the blue dashed box in (a); (d) Schematic diagram of grain size transition in surface topography of the sample prepared by SLSP)

3.2. Analysis of hydrophobic properties

Fig.5 shows the contact angles of the prepared samples under different processing conditions. The contact angle test was carried out directly after the samples were subjected to laser shock. The sample prepared under different process conditions were all in the hydrophilic state. By observing Sub-Fig (a), we could find that the static contact angles of the samples under different processing conditions were different before the low surface energy reagent was not coated. The hydrophobic angle of the sample corresponding to SLSP was the smallest, the hydrophobic angle of the sample corresponding to ALSP was the second, and the hydrophobic angle of the sample corresponding to NLSP was the largest. With the increase of the mesh size of the thin metallic mesh, the contact angle of the sample gradually decreased. By comparing Sub-Fig (a) and Sub-Fig (b), the sample changed from the initial hydrophilic state to the hydrophobic state after being modified by surface chemical reagents. By comparing the contact angles of samples prepared under different processing conditions, the hydrophobic angle of the sample corresponding to SLSP was the largest, the hydrophobic angle of the sample corresponding to ALSP was the second, and the hydrophobic angle of the sample corresponding to NLSP was the smallest. With the increase of the mesh size of the thin metallic mesh, the contact angle of the sample increased gradually. After the surface was treated with friction and wear, the static contact angles of the samples prepared under different processing conditions decreased to varying degrees. However, compared with the samples prepared by ALSP and NLSP, the static contact angle of the samples prepared by SLSP was still dominant. When the mesh size of the thin metallic mesh gradually increased, the static contact angle of the sample increased from 147.99±2.6 °to 152.49±2.3 °.

Preprints (www.preprints.org) | NOT PEER-REVIEWED | Posted: 18 April 2022 doi:10.20944/preprints202204.0171.v1

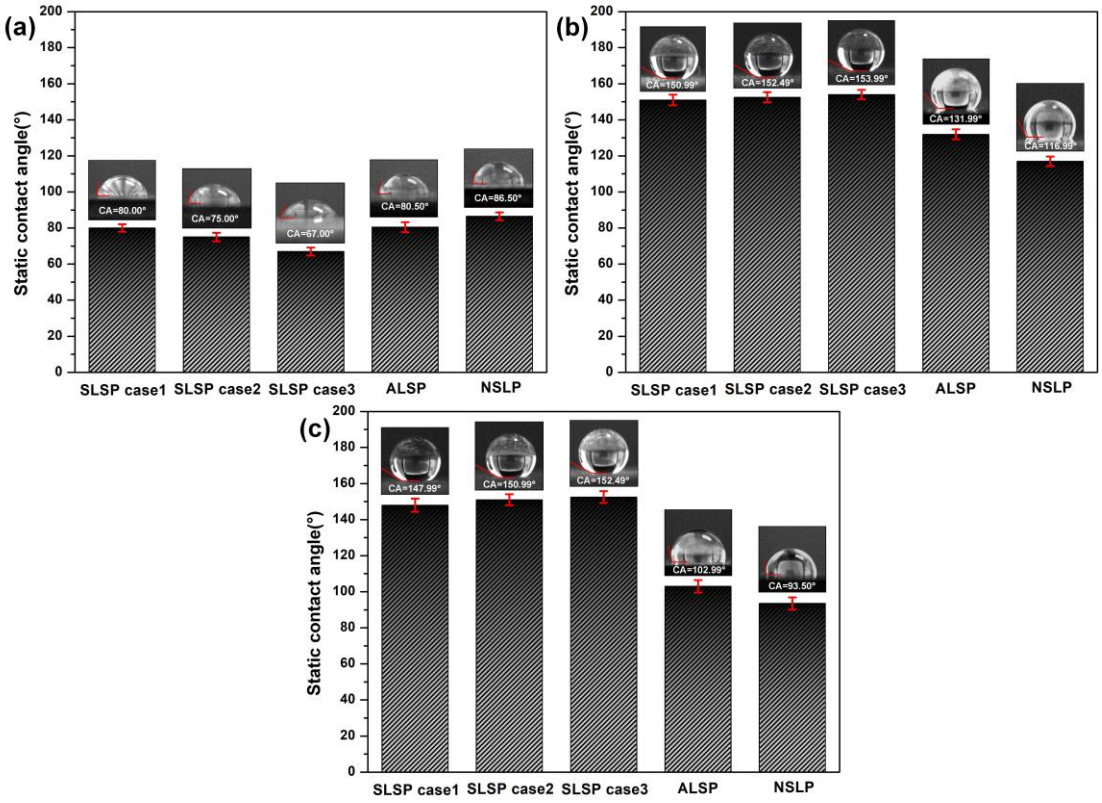

Fig.5. Contact angles of samples prepared under different processing conditions before and after chemical reagent modification

((a) Static contact angle of the sample before coating with chemical reagent; (b) Static contact angle of the sample after coating with chemical reagent; (c) Static contact angle of the sample after wear)

The macro-scale structure generated by laser shock and the micro-nano ablation structure formed a multi-level structure on the copper surface(**Fig.6**). These structures paved the way for the excellent hydrophobic properties of the surface of the material prepared by SLSP. We could evaluate the hydrophobic properties of smooth and chemically homogeneous material surfaces through static contact angle tests based on Young's model. The expression of Young's model is shown in Equation 1:

$$\cos(\theta) = \frac{\gamma_{sv} - \gamma_{sl}}{\gamma_{lv}} \tag{1}$$

Where γ was used to representing the surface tension, the energy per unit area on the interface. The tables *sv*, *lv*, and *sl* represented the solid-gas, liquid-gas, and solid-liquid interfaces. The model provided a correlation between static contact angle and interfacial tension. The contact angle in Young's model resulted from the thermodynamic equilibrium of free energy at the solid-liquid-vapor interface. However, this model was only suitable for ideal solid surfaces and was not valid for surfaces with dual-scale roughness and chemical inhomogeneity. Water droplets on surfaces with dual-scale roughness may exist in two states. One was the Wenzel state, where water droplets can penetrate the structure. The second was the Cassie-Baxter state, where water droplets were suspended above the periodic structure(**Fig.6(c)**). When in the Wenzel state, the droplet filled the rough grooves on the solid surface, causing the actual wetted total surface of the

Preprints (www.preprints.org) | NOT PEER-REVIEWED | Posted: 18 April 2022 doi:10.20944/preprints202204.0171.v1

droplet to be larger than the projected area. Therefore, the hydrophobic properties corresponding to the above-mentioned interfacial state were increased compared to the smooth surface. The apparent contact angle of the solid surface corresponding to the Wenzel state could be expressed as[24]:

$$\cos(\theta^*) = r_f \frac{\gamma_{sv} - \gamma_{sl}}{\gamma_{lv}} = r_f \cos(\theta) \quad (2)$$

In the formula, r_f was the roughness coefficient of the solid surface. The ratio of the area of the actual surface of the solid to the area of the projected surface. When in the Cassie-Baxter state, the gaseous medium filled the rough grooves on the solid surface, so the droplets wetted the solid surface. The interface state changed from a solid-liquid interface to a combination of a solid-liquid-gas interface. The apparent contact angle corresponding to the Cassie-Baxter state could be expressed by[25]:

$$\cos(\theta^{**}) = r_f f \cos(\theta) + f\text{-}1 \quad (3)$$

where f is the area fraction of the solid surface. The above equation showed that the geometry of the solid surface had an important influence on the hydrophobic properties of the material under the same coating process of the low surface energy material. Compared with the original samples without laser shock, the different contact formed between solids and droplets (solid-liquid contact or solid-gas-liquid contact) after laser shock was the main factor affecting the material's hydrophobic properties surface. For the ALSP-treated samples, the droplets quickly infiltrated the bottom of the gully of the crater, meeting the requirements of the Wensel wetting model. However, for the samples treated by SLSP, more bottomless pits were formed on the sample's surface due to the macroscopic plastic deformation. Many periodic micro-nano hierarchical structures were developed, which met the requirements of the Wensel wetting mode. According to the Wenzel model, there was a close relationship between the hydrophobicity and surface roughness before coating with low surface energy substances. The experimental results in Figures 3 and 6 verified the model's accuracy. With the increase in the surface roughness of the sample, the wettability of the sample improved, and the static contact angle decreased. According to the Cassie-Baxter model, the hydrophobicity of the material was related to the actual liquid-solid contact area after coating with low surface energy substances. The calculation results of the micro-pit volume in Section 3.1 showed that within the same surface area, the micro-pit volume on the surface of the sample prepared by the large-scale thin metallic mesh was the largest. The larger the volume of the micro-pit, the more gas was stored inside the pit, which made the actual contact area of solid-liquid more minor. Therefore, with the increase of the mesh size of the thin metallic mesh, the contact angle of the sample increased.

Preprints (www.preprints.org) | NOT PEER-REVIEWED | Posted: 18 April 2022 doi:10.20944/preprints202204.0171.v1

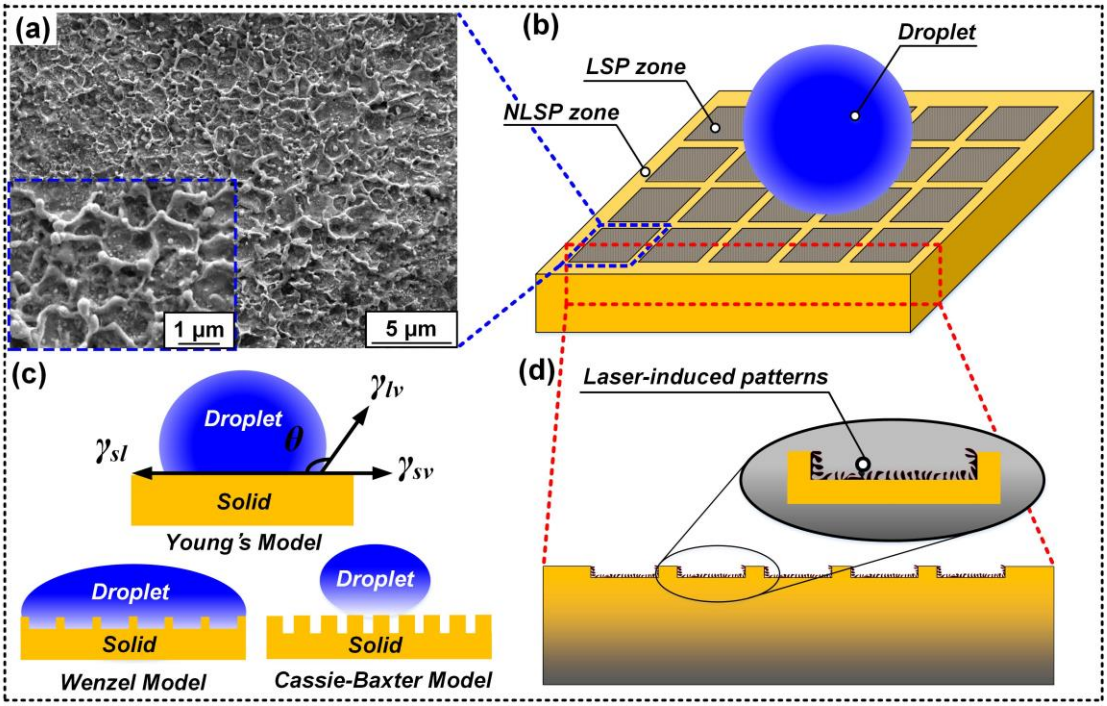

Fig.6. Schematic diagram of the surface and cross-sectional structure and hydrophobic model of the materials prepared by SLSP

((a) SEM. image of micro-nano topography produced by laser shock; (b) Schematic diagram of hydrophobicity of samples prepared by SLSP; (c) Schematic diagram of the hydrophobic theoretical model; (d) Schematic diagram of the micro-nano topography produced by laser shock)

3.3. Analysis of hardness properties

Fig.7 showed the hardness distribution in the horizontal direction of the samples prepared by SLSP. The three data points with distance = 0 in Sub-Fig (a) corresponded to the hardness values of the material under the thin metallic mesh with different mesh sizes. After comparison, the hardness value of the material under the thin metallic mesh corresponding to SLSP/case1 was the highest, SLSP/case2 was second, and SLSP/case3 was the lowest. When the laser was irradiated on the surface of the thin metallic mesh, plasma was induced, and pressure shock waves were excited. The stress wave would propagate along the material thickness direction under the confinement of the surface confinement layer. However, the stress wave decayed as it propagated downward. Table 2 gives the thickness dimension of thin metallic mesh in cases 1~3. With the increase of the mesh size, the mesh diameter of the thin metallic mesh gradually increased, making the peak pressure of the stress wave transmitted to the surface of the sample through the thin metallic mesh decrease progressively. The three data points of distance = -75 and distance = 75 in Sub-Fig (a) corresponded to the hardness values of the material under the mesh holes of the thin metallic mesh of three different mesh sizes, respectively. Compared with the hardness value of the material directly covered by the thin metallic mesh, the hardness value of the material surface directly irradiated by the pulsed laser was more considerable with the increase of the mesh size of the thin metallic mesh. In this area, the pulsed laser was directly irradiated on the surface of the copper material increases in the same area. The direct interaction between the laser and the material would induce plasma and generate plasma pressure waves, which excited huge surface waves. The surface waves under the adjacent thin metallic mesh would interfere. The interfering surface waves would aggravate the plastic deformation of the surface, thereby refining the grains

Preprints (www.preprints.org) | NOT PEER-REVIEWED | Posted: 18 April 2022 doi:10.20944/preprints202204.0171.v1

and improving the hardness of the material. **Fig.8** showed the hardness distribution in the longitudinal direction of the samples prepared by SLSP. Similarly, with the increase of the mesh size of the thin metallic mesh, the interference effect of the surface wave was enhanced, which increased the plastic deformation degree at the same position in the longitudinal direction of the material, the grain size decreased, and the hardness value of the material increased. Since the laser-induced stress wave would be attenuated in the process of propagation in the thickness direction, the hardness values of different regions in the material thickness direction differed, and the hardness value gradually decreased along the material thickness direction. At the same time, the displacement of the pressed-in specimen surface in the Sub-Fig (a)-(c) in Fig. 6-7 could also indirectly reflect the hardness values in different regions of the material.

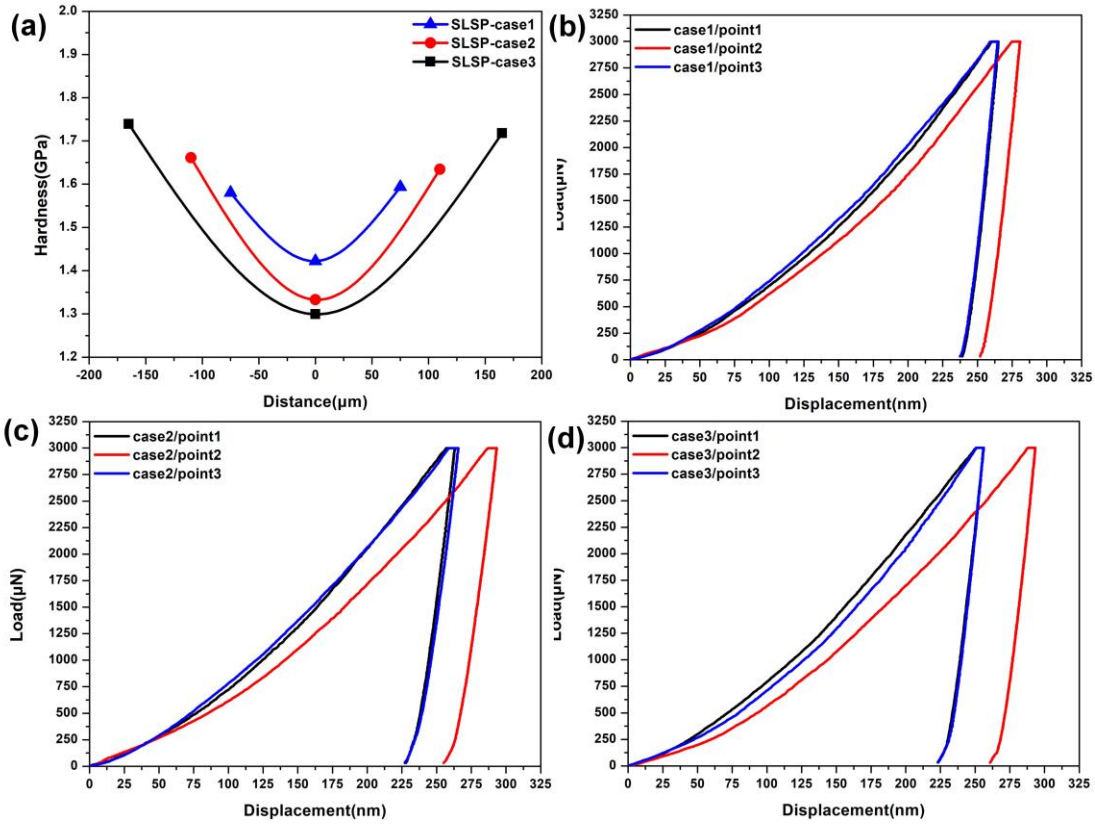

Fig.7. Hardness distribution in the horizontal direction of the samples prepared by SLSP ((a)Hardness distribution of sample in the horizontal direction; (b)Force-displacement curve corresponding to SLSP/case 1; (c)Force-displacement curve corresponding to SLSP/case 2; (d)Force-displacement curve corresponding to SLSP/case 3)

Preprints (www.preprints.org) | NOT PEER-REVIEWED | Posted: 18 April 2022 doi:10.20944/preprints202204.0171.v1

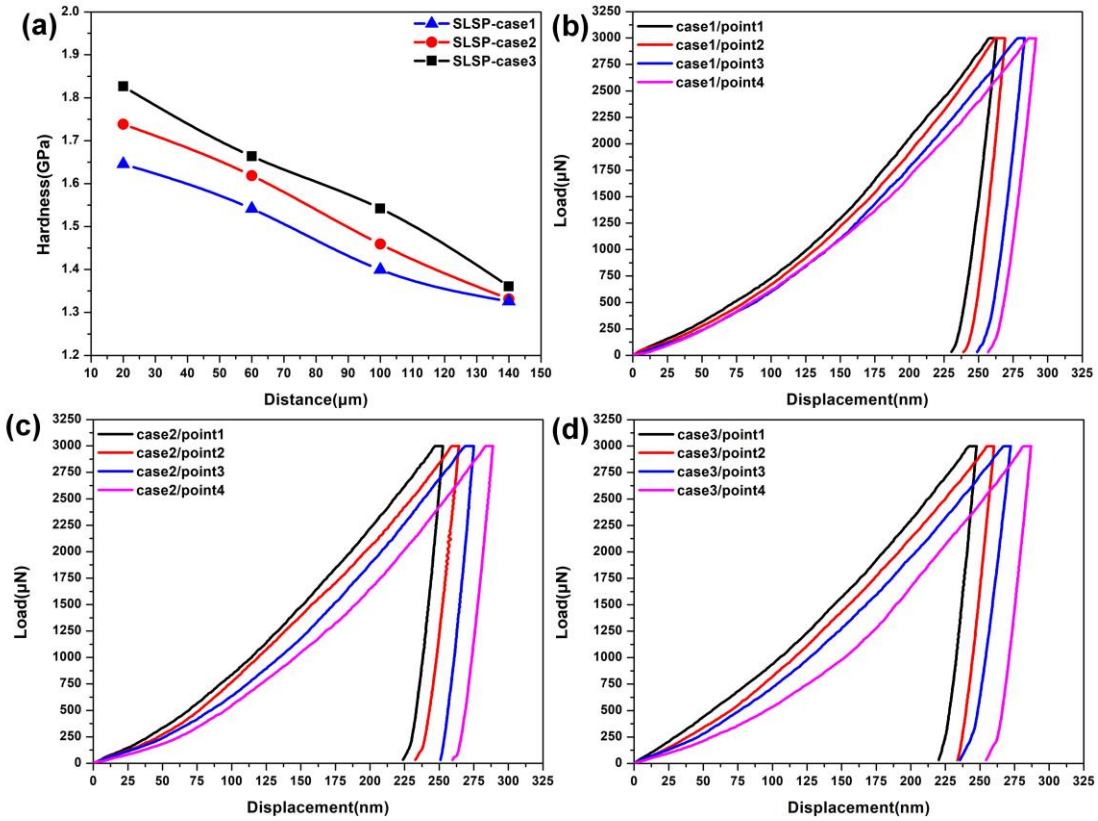

Fig.8. Hardness distribution in the longitudinal direction of the samples prepared by SLSP ((a)Hardness distribution of sample in the longitudinal direction; (b)Force-displacement curve corresponding to SLSP/case 1; (c)Force-displacement curve corresponding to SLSP/case 2; (d)Force-displacement curve corresponding to SLSP/case 3)

The microhardness of metal was closely related to the microstructure and residual stress. The grain size of copper changed after laser shock operation. Combined with the T.E.M. morphologies of samples prepared by SLSP in **Fig.9**, we elaborated the grains' plastic deformation mechanism induced by laser shock. First, the dislocations inside the original grains started to move, producing dislocation lines. With the further accumulation and development of dislocation lines, twins and high-density dislocations were generated inside the grains. When the dislocations accumulated to a certain extent, dislocation walls and entanglements appeared inside the grains. When the amount of deformation strain reached a certain level, that was, when the dislocation density in the dislocation wall and dislocation entanglement reached a specific upper limit, these dislocations began to annihilate and rearrange to form subgrain boundaries. At the same time, the subgrain boundaries subdivided the original coarse grains into various subgrains to form refined grains. Since the pressure wave would gradually attenuate in the process of downward transmission, the deformation strain of the grains in the thickness direction of the material was different. Then a strain gradient would be generated, resulting in a structure with a grain size gradient along the thickness direction. According to the classical Hall-Petch formula[26], there was a correlation between pure metallic materials' grain size and strength. This formula presented the relationship between the initial yield point and grain size.

$$\sigma_y = \sigma_0 + k\frac{1}{\sqrt{D}} \tag{4}$$

Preprints (www.preprints.org) | NOT PEER-REVIEWED | Posted: 18 April 2022 doi:10.20944/preprints202204.0171.v1

Where σ_y was the initial yield point of the material; D was the grain size of the material; σ_0 is a constant related to the chemical composition; k was a constant related to the microstructure. From Equation 4, the refined grains with smaller grain sizes had higher strength values than coarse grains with large grain sizes could be concluded. Compared with the material area covered with thin metal mesh, when the laser directly interacted with the material's surface without the thin metallic mesh, the plasma pressure shock wave would have a more substantial punching effect on the material surface and a higher degree of grain refinement. For the metal area directly affected by the laser, with the increase of the mesh size of the thin metal mesh, the intensity of the plasma pressure wave excited by the laser and the material was higher, so the grain size of the material was refined more. For the thin metal area that was not directly acted on by the laser, as the mesh size of the thin metal mesh increased, the thickness of the thin metal mesh also increased. Since the pressure wave would gradually attenuate during the downward propagation through the metal mesh, this led to a decrease in the intensity of the pressure wave indirectly acting on the surface of the metal target. The substrate's grain size was reduced, and the strength of the material was reduced, resulting in a reduction in the hardness value of the material.

The relationship between material microhardness and microstructure was as follows[27–29]:

$$H = H_0 + \alpha G b p \tag{5}$$

where H_0 was the hardness value of the material in the ideal state (without internal defects), α was the constant of the material, G was the shear modulus, b was the Burgers vector, and p was the average dislocation density. There was also a relationship between dislocation density and twin spacing, as shown in the following formula[27-29]:

$$p=\Delta\theta/(db) \tag{6}$$

where $\Delta\theta$ was the off-angle caused by excess dislocations and d was the twin spacing. Therefore, the correlation between H and d was as follows[27-29]:

$$H = H_0 + \alpha G b \Delta\theta/(db) \tag{7}$$

Therefore, from the above formula: with the decrease of the twinning spacing, the dislocation density increased, and the hardness increased. The simulation calculation results of molecular dynamics in **Fig.10** also showed that in the process of laser shock copper, with the increase of the material strain rate, the thickness of the internal twin layer of the material decreased. Comparing Sub-Fig.10(a) with Sub-Fig.10(c), Laser shock could significantly reduce the thickness of the twin space inside the grain. The numerical simulation results of molecular dynamics and the photographed TEM results were also consistent with the deduction of the theoretical formula.

Preprints (www.preprints.org) | NOT PEER-REVIEWED | Posted: 18 April 2022 doi:10.20944/preprints202204.0171.v1

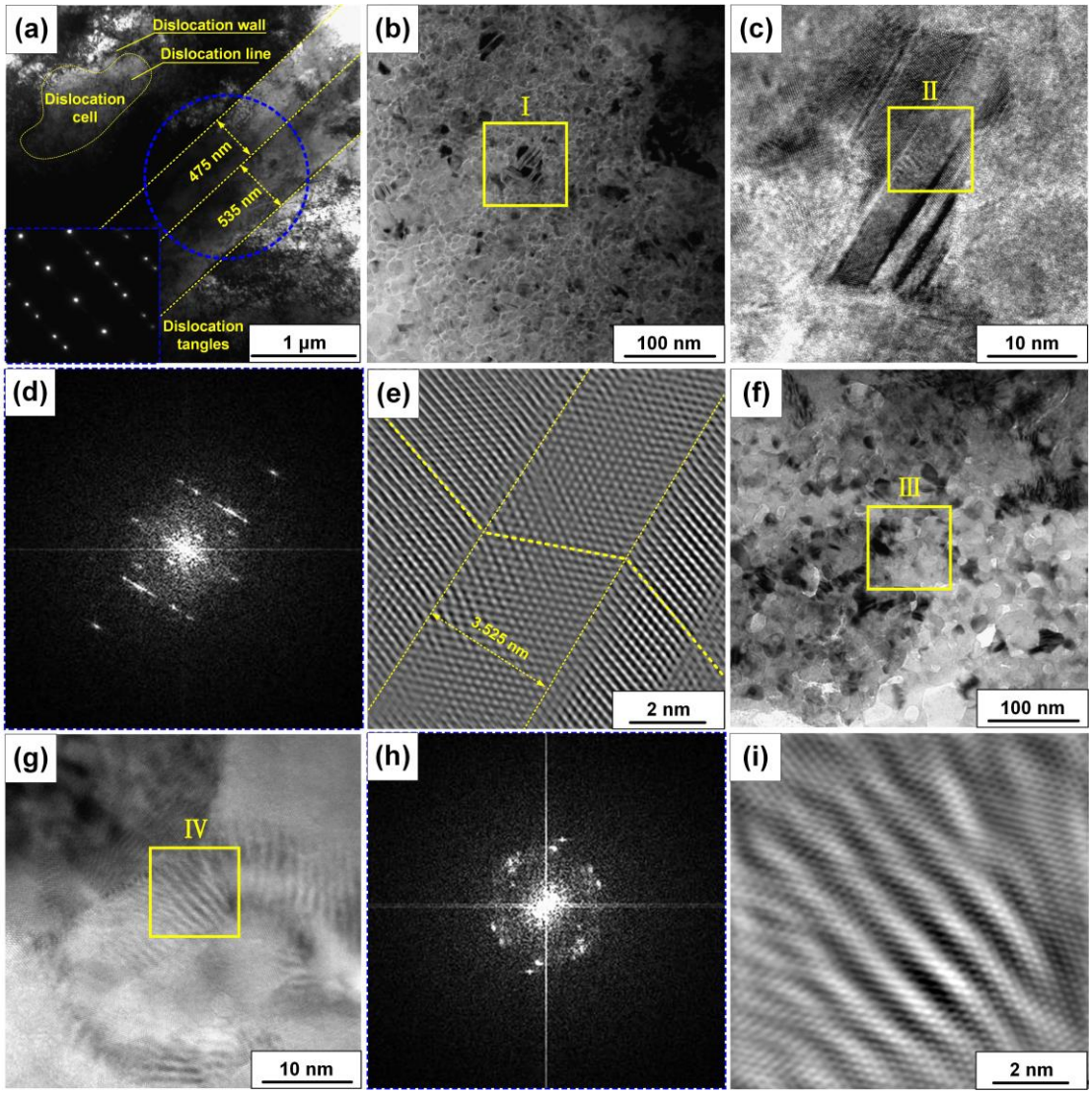

Fig.9. TEM morphologies of samples prepared by SLSP

((a) TEM transmission image of the original annealed sample; (b) TEM transmission images of ultrafine grains prepared by SLSP; (c) HRTEM of region I in Sub-Fig (b); (d) Selected area electron diffraction pattern of region II in Sub-Fig (c); (e) IFFT image of the Sub-Fig (d); (f) TEM transmission images of fine grains prepared by SLSP; (g) HRTEM of region III in Sub-Fig (f); (h) Selected area electron diffraction pattern of the IV region in Sub-Fig (g); (i) IFFT image of the Sub-Fig (h)

Preprints (www.preprints.org) | NOT PEER-REVIEWED | Posted: 18 April 2022 doi:10.20944/preprints202204.0171.v1

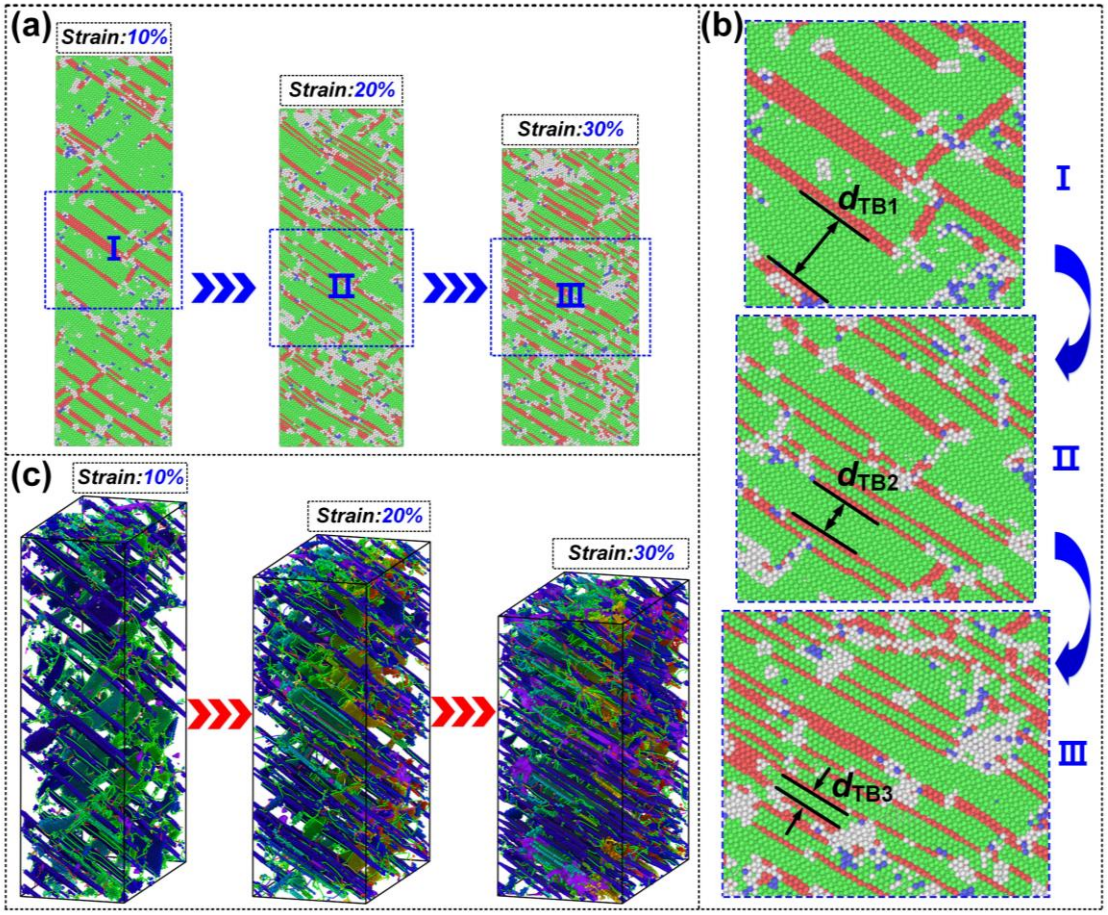

Fig.10. Influence of dynamic laser shock peening process on twin spacing
((a) Plan view of twin distribution during laser shock-induced plastic deformation of materials; (b) Partially enlarged view of the blue dashed box in Sub-Fig (a); (c) Three-dimensional view of twin distribution during laser shock-induced plastic deformation of materials; d_{TB1}-d_{TB3} were the twin space corresponding to strain rates of 10%-30%, respectively)

There was a certain relationship between residual stress and microhardness. Residual tensile stress would decrease hardness, and the residual compressive stress would increase hardness[30]. Based on the microscopic properties and hardness data of the material obtained from the experiment, we calculated the residual stress of the specimen corresponding to SLSP. **Fig.11** showed the residual stress distribution of the samples prepared by SLSP. **Fig.12** showed the XRD patterns of samples under different processing conditions. The plane residual stress nephogram corresponded to the part corresponding to the black dotted line in the three-dimensional residual stress nephogram. We could observe in **Fig.11** that most of the regions in the specimen exhibited residual compressive stress. It was worth noting that the material below the covered area of the thin metallic mesh, which was not directly affected by the laser beam, also exhibited residual compressive stress. Compared with the copper material covered with the metal mesh, the copper without the metal mesh had a high residual compressive stress value. It showed that the stress wave generated by the pulsed laser still impacted the material after being transmitted to the sample's surface through the thin metallic mesh. In addition, the surface waves caused by adjacent laser shock waves interfered with each other, which also increased the hardness of the area not directly affected by the laser shock waves. By comparing the Sub-Fig (a) - (c), the peak residual

 doi:10.20944/preprints202204.0171.v1

compressive stress of the samples was different. The residual compressive stress of the sample corresponding to case 1 was the smallest, the residual compressive stress of the corresponding sample of case2 was second, and the residual compressive stress of the corresponding sample of case3 was the largest. In the same irradiation area, with the increased mesh size of the thin metallic mesh, the area of the copper material directly irradiated by the pulsed laser increased, the interference effect of the adjacent surfaces gradually increased, and the residual compressive stress steadily increased. We could observe in **Fig.12** that the spectra of the samples prepared under different processing conditions were similar. And the sample only had a single Cu phase, and no noticeable oxidation was observed. After local amplification of the diffraction spectrum corresponding to the (111) crystal plane, the diffraction peaks of the (111) crystal plane of the samples corresponding to ALSP and SLSP were shifted to different degrees compared with the samples corresponding to NLSP. The half-peak widths of the samples prepared under different processing conditions were different. The FWHM of the ALSP sample was the largest, followed by the SLSP sample, and the NLSP sample was the smallest. As the mesh size of the thin metal mesh increased, the half-width of the sample increased gradually. Since the interplanar spacing would change with residual stress in the sample, the resulting diffraction peak would also move when Bragg diffraction occurs. Residual compressive stress decreased the interplanar spacing, resulting in a shift of the diffraction peaks to high angles[31]. The diffraction peak of the (111) crystal plane of the sample corresponding to ALSP was the most shifted, followed by SLSP. With the increase of the mesh size of the thin metallic mesh, the shift of the (111) crystal plane diffraction peak gradually increased. The XRD test results were consistent with the simulation data, which also verified the validity of the numerical model. The change of material hardness was the comprehensive performance of material microstructure (grain size, dislocation density, twin spacing) and stress state. Selective laser shock improves the hardness of the material, which undoubtedly makes a beneficial contribution to the improvement of the tribological properties of the material.

Preprints (www.preprints.org) | NOT PEER-REVIEWED | Posted: 18 April 2022 doi:10.20944/preprints202204.0171.v1

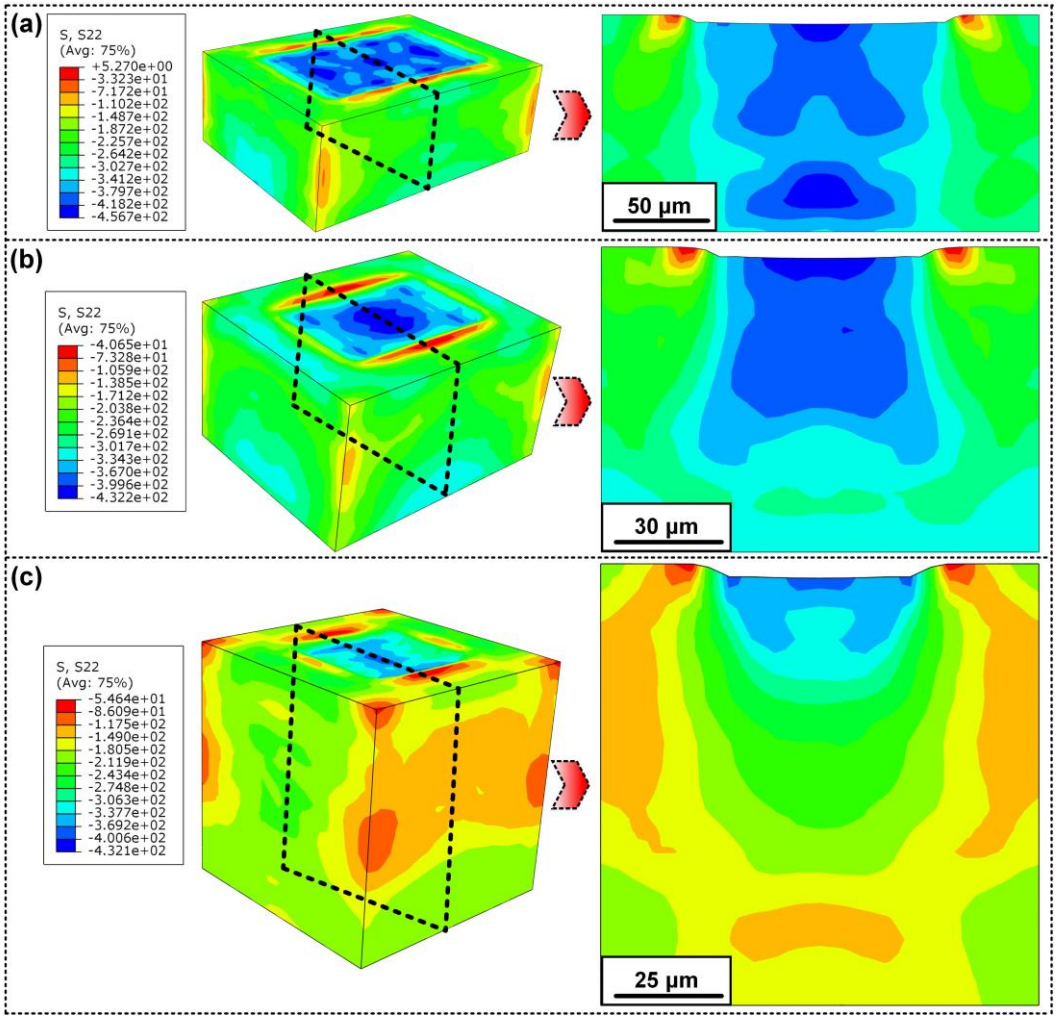

Fig.11. Residual stress distribution of the samples prepared by SLSP
((a)~(c) correspond to the residual stress distribution of samples in case1~3, respectively)

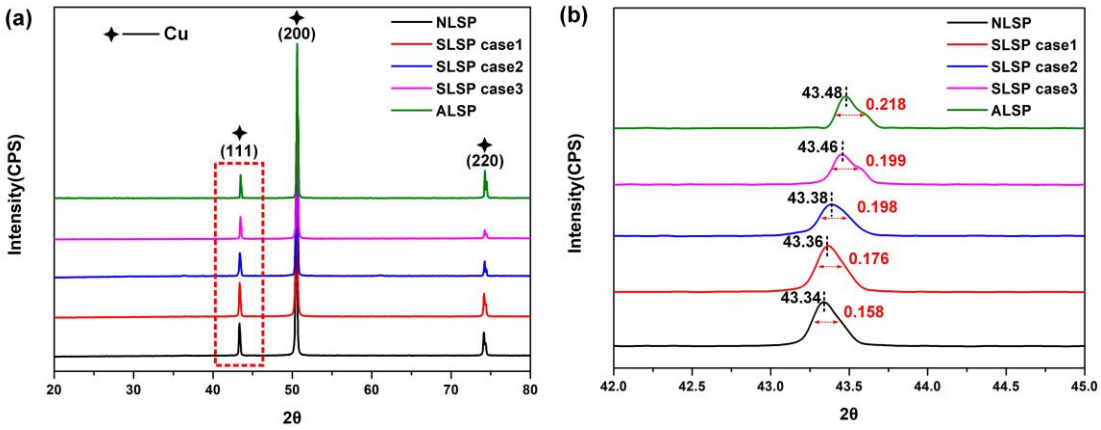

Fig.12. XRD patterns of samples under different processing conditions
((a) Overall picture; (b) Partial magnification picture in red dotted box)

Preprints (www.preprints.org) | NOT PEER-REVIEWED | Posted: 18 April 2022 doi:10.20944/preprints202204.0171.v1

3.4. Analysis of tribological properties

Fig.13 showed the tribological properties of samples under different processing conditions. Observing the Sub-Fig (a), the friction coefficient curves of the samples prepared under different processing conditions obtained from the friction and wear experiments had similar trends. With the start of the friction test, the friction factor of the sample increased rapidly. When the friction process was stable, the friction coefficient of the sample was gradually stable. With the end of the friction test, the friction factor of the sample dropped rapidly. However, it was worth noting that under different processing conditions, the numerical value of the friction factor of the sample and the fluctuation of the friction factor curve were different. The sliding friction factor of the sample was related to the sample's mechanical properties. Compared with the NLSP sample (the friction coefficient was about 0.83), the friction coefficient of the SLSP sample was significantly reduced by about 0.68. Compared with the friction coefficient curve of the SLSP sample, the band amplitude of the friction coefficient curve of the NLSP sample was larger, which could also be indirectly stated that the SLSP sample has better tribological stability than the NLSP sample. The experimental data showed that laser shock could effectively reduce the sliding friction coefficient of the material. The Sub-Fig (b) and (c) could reflect the wear condition of the samples under different processing conditions. Compared with the NLSP sample, the SLSP sample had a smaller wear scar depth and a lower wear rate. The wear scar morphology of the samples prepared under different processing conditions was different, and the solid wear mechanism was also different. For the original sample without laser shock, there were many deep plows inside the wear scar and large peeling pits, showing a typical composite wear mechanism of abrasive wear and fatigue wear(Sub-Fig (d) and (e)). Compared with the original sample without laser shock, after the interaction between the pulsed laser and the material, the material's surface would be ablated. The degree of oxidation of the surface layer of the material would be increased**(Fig.S4)**[32,33]. Both the laser-induced hardened layer and the newly generated hard oxide layer could effectively improve the tribological properties of the material. For the samples prepared by SLSP, the wear mechanism was a composite wear mechanism of fatigue wear, abrasive wear, and oxidative wear(Sub-Fig (f) and (g)). Due to the interaction between the surface of the sample and the dual ball during the wear process, extensive plastic deformation occurred, and fatigue microcracks were formed. With the further expansion of the crack, a through crack was formed, which made the surface material detach from the matrix and peel off, including a peeling pit. For the SLSP sample, there were many micro-pits on the surface. During wear, the wear debris acted as a lubricant. The pits on the surface of the SLSP sample served as lubricant storage(Sub-Fig (h), which made the samples corresponding to SLSP have better tribological properties than the samples of NLSP.

Preprints (www.preprints.org) | NOT PEER-REVIEWED | Posted: 18 April 2022 doi:10.20944/preprints202204.0171.v1

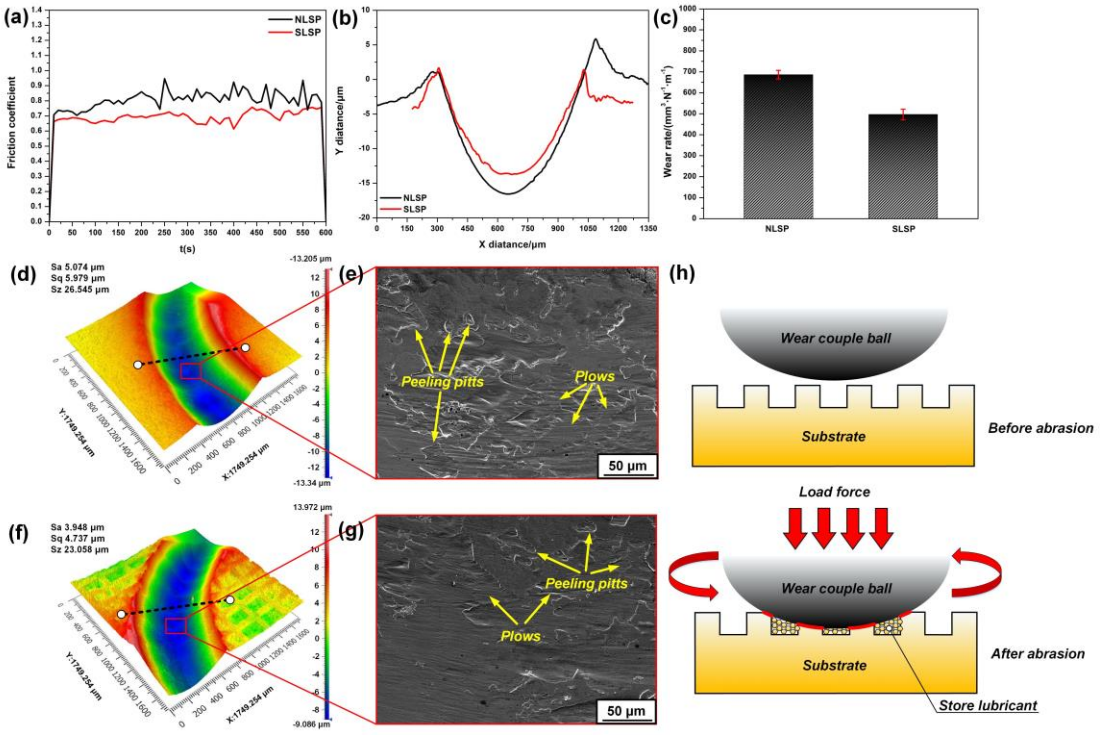

Fig.13.Tribological properties of samples prepared by SLSP

((a) Friction coefficient curves of samples under different processing conditions; (b) 2D profile of wear scars of NLSP sample; (c) Wear rate of samples under different processing conditions; (d) 3D profile of NLSP sample; (e) SEM morphology of wear scars of NLSP sample; (f) 3D profile of wear scars of SLSP sample; (g) SEM morphology of wear scars of SLSP sample; (h) Schematic diagram of wear process of SLSP sample)

3.5. Analysis of tensile properties

Fig.14 showed the tensile property of samples under different processing conditions. Observing and comparing the Sub-Fig (a)-(b), the variation trends of the tensile curves of the samples prepared under different processing conditions were similar. They all showed typical tensile curve characteristics. There were four different stages: elastic stage, yield stage, strain hardening stage, and necking fracture stage. Comparing the yield strength and uniform elongation of tensile specimens under different processing conditions, the uniform elongation of the sample corresponding to NLSP was the largest, and the yield strength was the smallest. The uniform elongation of the specimen corresponding to ALSP was the smallest, and the yield strength was the largest. As the mesh size of the thin metallic mesh increased, the yield strength of the tensile specimen increased, and the uniform elongation decreased. It was worth noting that the uniform elongation of the case1 specimen prepared by the SLSP process was 43%, and the yield strength was 96 MPa, while the uniform elongation of the original sample was 45%, and the yield strength was 59 MPa. The results of tensile experiments showed that the SLSP process could significantly improve the yield strength of the material without sacrificing its ductility of the material. Sub-Fig (c) showed the tensile properties of copper materials under specific processing techniques reported in references[34,35]. We could find that tensile property equivalent to or better than those prepared by the processing methods in ref. It could be achieved using the SLSP process. The SLSP process produced an alternating regular distribution of hard and soft phases on the material's surface. This regular distribution of soft and hard phases will benefit the material's tensile

Preprints (www.preprints.org) | NOT PEER-REVIEWED | Posted: 18 April 2022 doi:10.20944/preprints202204.0171.v1

properties. To verify this conjecture, we established theoretical numerical models of samples under different processing conditions based on the idea of finite element. The tensile properties of samples with alternately regularly distributed soft and hard phases, randomly distributed soft and hard phases, all hard phases, and all soft phases were studied, respectively. Sub-Fig (d) showed the simulation results of the tensile curves under different processing conditions. If the material's surface was all hard phases, although the material itself had excellent tensile strength, the ductility of the material itself was sacrificed. If the material's surface was all soft phase, although the material's ductility increased, the yield strength of the material itself decreased. Compared with the above two cases, when there were hard and soft phases on the material's surface, the yield strength of the material could be increased within a specific range without significantly sacrificing the ductility of the material. It was worth noting that, compared with the random distribution of the soft and hard phases, when the soft and hard phases were alternately and regularly distributed, the material had better ductility under the premise of ensuring approximately the same strength. Since twins were not considered in the calculation model, the strength and ductility data obtained by the simulation calculation were lower than the experimental data.

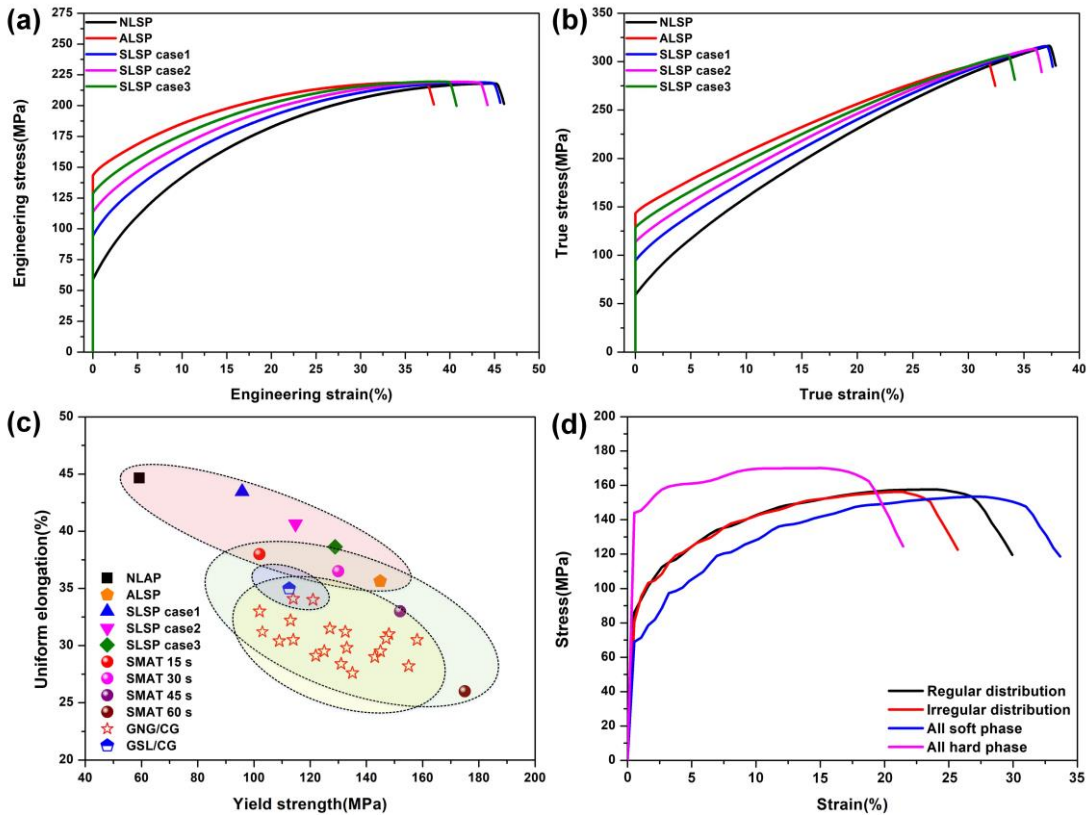

Fig.14. Tensile property of samples under different processing conditions.
((a) True stress-true strain curves of tensile samples under different processing conditions; (b) Engineering stress-engineering strain curves of tensile samples under different processing conditions; (c) Correlation between yield strength and uniform elongation of tensile samples under different processing conditions; (d) Simulation results of the tensile curves under different processing conditions)

Fig.15 showed the initial tensile state of the samples corresponding to different processing conditions. Combined with **Fig.S10** and **Fig.15**, the necking forms of the samples prepared under

Preprints (www.preprints.org) | NOT PEER-REVIEWED | Posted: 18 April 2022 doi:10.20944/preprints202204.0171.v1

different processing conditions were different. According to the order of necking time, the samples with "all hard phases" had necking first, followed by the samples with "two-phase and irregular distribution." The "two-phase and regularly distributed" sample was in the third place, and the "all soft phase" sample was the last to appear necking. The hard phase region was the necking position of the "two-phases and regularly distributed" samples. The soft phase region was the necking position of the "two-phases and irregularly distributed" sample. Substantial shear stress was one of the main factors of tensile failure of metallic materials. If the necking caused by the localized strain were earlier than the overall plastic deformation of the specimen, the shear band inside the material would directly evolve into a through the crack, which would eventually lead to the failure of the material. On the one hand, the metal material with gradient structure prepared by SLSP realized the transition of the grain size from the uppermost nanoscale to the inner micro-scale. On the other hand, the transition of nanoscale grains in the surface hard phase region to micro-scale grains in the soft phase region was realized. This ordered distribution of grain sizes could induce macroscopic strain gradients and transform unidirectional stress into multiaxial stress due to incompatible deformations evolving along the gradient direction. As a result, strain localization could be reduced, and unique anomalous strain hardening could be achieved, resulting in higher ductility. This 3D gradient structure enabled the samples prepared by SLSP to obtain more significant mechanical properties of strong-plastic synergy compared with the 2D structure. When the deformation of the material exceeded the elastic deformation range, the material's behavior was plastic deformation. This model obeyed the Von Mises yield criterion[36]:

$$\sigma_e = \frac{1}{\sqrt{2}}\sqrt{(\sigma_1-\sigma_2)^2+(\sigma_2-\sigma_3)^2+(\sigma_3-\sigma_1)^2} < \sigma_\gamma \quad (8)$$

where σ_1, σ_2, and σ_3 were the principal stresses of the first, second and third, respectively. σ_γ was the yield stress, including a safety factor. Compared with the randomly distributed strengthening phase (hard phase), the regularly distributed strengthening phase (hard phase) could increase the tensile stress in the other two directions. Therefore, earlier strain localization or early necking due to defect accumulation could be avoided, improving the ductility of the material.

Preprints (www.preprints.org) | NOT PEER-REVIEWED | Posted: 18 April 2022 doi:10.20944/preprints202204.0171.v1

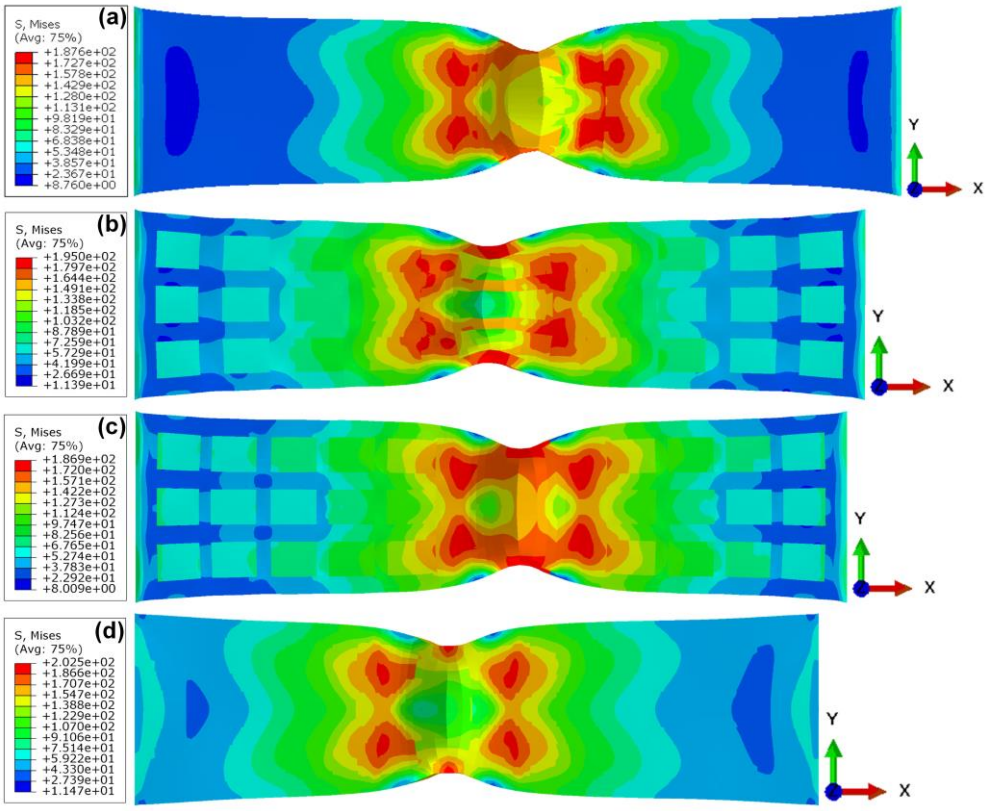

Fig.15 Necking state of the samples corresponding to different processing conditions ((a) All soft phase;(b) Regular distribution;(c) Irregular distribution;(d) All hard phase)

In traditional metal materials, strength and ductility were considered a pair of contradictions. However, metals with grain size gradients have become a research hotspot in recent years due to their potential for synergistic effects of strong plasticity. Laser shock was one of the techniques for producing metal materials with gradient structure distribution. After laser shock treatment, the material's grain size expanded from the nanometer level on the surface to the micrometer level inside. According to structural mechanics, the orderly arrangement of the grain size gradient of the material itself could induce a macroscopic strain gradient, realize the transformation from uniaxial stress to multiaxial stress, reduce strain localization, and obtain higher ductility[37]. According to the mechanics of materials, the deformation mechanisms of materials in different regions were different, and the critical stress and strain required for dislocation activation were also different. This gradual deformation process could effectively avoid the long-range accumulation of dislocations, thereby suppressing the localization of shear bands. In the gradient-structured metals produced by laser shock, the deformation of nanocrystalline copper was dominated by mechanically driven grain boundary migration, accompanied by grain coarsening and softening. Meanwhile, the deformed coarse grains were hardened by dislocation slip and stacking, providing work hardening of the bulk sample. Coarse grains inside the material contributed to good ductility, and fine grains on the material's surface provided good strength. This combination of cross-scale grains resulted in materials with excellent strength and ductility.

The yield strength of copper material was closely related to the corresponding grain size and twin spacing of the material. The interaction of dislocations and twins was considered the primary mechanism of strengthening, strain hardening, and toughening of nanotwinned copper. Lattice dislocations usually nucleated from free surfaces or grain boundaries, and upon further plastic

 doi:10.20944/preprints202204.0171.v1

deformation, twin grain boundaries could serve as additional dislocation sources. The increase in yield stress of nanotwinned copper was mainly due to the pinning effect of twinned grain boundaries on dislocations. In the twin layer scale range of 0-40 nm, the yield strength of the material decreased with the increase of the twin layer spacing[38]. Laser shock could effectively reduce the twinned interlayer spacing and form a structure with a gradient of the twinned interlayer spacing in the material thickness direction, thereby producing a metal structure with a gradient of mechanical properties along the material thickness direction. Molecular dynamics simulation and TEM imaging results could also provide effective support (**Fig.9-10**).

However, for materials with a two-phase gradient distribution on the surface and gradients in microscopic and mechanical properties and their thickness, plastic deformation initially occurred in the coarse-grained system (soft phase). As the load increases, the plastic deformation gradually diffuses into the fine-grained system (hard phase). This three-dimensional gradient structure was quite different from the traditional two-dimensional gradient structure reported in references[34-36], that was, there was only a gradient transition in the material thickness direction. Compared with the traditional two-dimensional gradient structure, this ordered plastic deformation of the three-dimensional gradient structure could more effectively release the intergranular stress between adjacent grains of different sizes, thereby suppressing the strain localization. The tensile test results showed that the metal samples with the three-dimensional gradient structure had more excellent strength and ductility.

4. Conclusions

In this paper, the application scope of the laser shock wave is expanded. A novel technology of selective laser shock preparation of high-reliability hydrophobic surface structure is proposed using the self-armored multiscale surface morphology concept. The SLSP process could fabricate an array-like distribution of micro-pits on the material's surface, forming a multi-level hydrophobic structure across scales. Compared with the NLSP and ALSP samples, the hydrophobic properties of the SLSP samples are significant. Moreover, after mechanical wear, the surface of the structure prepared by SLSP still shows a superhydrophobic state. The SLSP process could prepare a 3D gradient structure material with a two-phase (strong phase, soft phase) distribution on the surface and a multi-level gradient distribution in the thickness direction. The SLSP process could use a single process to prepare a highly reliable surface structure with excellent hydrophobic properties, mechanical properties, and tribological properties, which have essential engineering application value.

Acknowledgments

This work was supported by the National Natural Science Foundation of China (Grant No. 51901162). The authors thanked the support of the Chinese National Talent Program.

References

[1] J. Wu, K. Yin, S. Xiao, Z. Wu, Z. Zhu, J.A. Duan, J. He, Laser Fabrication of Bioinspired Gradient Surfaces for Wettability Applications, Adv. Mater. Interfaces. 8 (2021) 1–23. https://doi.org/10.1002/admi.202001610.

[2] M. Yeganeh, N. Mohammadi, Superhydrophobic surface of Mg alloys: A review, J. Magnes. Alloy. 6 (2018) 59–70. https://doi.org/10.1016/j.jma.2018.02.001.

[3] W. Zhang, D. Wang, Z. Sun, J. Song, X. Deng, Robust superhydrophobicity: Mechanisms and strategies, Chem. Soc. Rev. 50 (2021) 4031–4061. https://doi.org/10.1039/d0cs00751j.

[4] D. Wang, Q. Sun, M.J. Hokkanen, C. Zhang, F.Y. Lin, Q. Liu, S.P. Zhu, T. Zhou, Q. Chang, B. He, Q. Zhou, L. Chen, Z. Wang, R.H.A. Ras, X. Deng, Design of robust superhydrophobic surfaces, Nature. 582 (2020) 55–59. https://doi.org/10.1038/s41586-020-2331-8.

[5] X. Meng, M. Wang, L. Heng, L. Jiang, Underwater Mechanically Robust Oil-Repellent Materials: Combining Conflicting Properties Using a Heterostructure, Adv. Mater. 30 (2018) 1–8. https://doi.org/10.1002/adma.201706634.

[6] K. Ellinas, A. Tserepi, E. Gogolides, Durable superhydrophobic and superamphiphobic polymeric surfaces and their applications: A review, Adv. Colloid Interface Sci. 250 (2017) 132–157. https://doi.org/10.1016/j.cis.2017.09.003.

[7] L.R.J. Scarratt, U. Steiner, C. Neto, A review on the mechanical and thermodynamic robustness of superhydrophobic surfaces, Adv. Colloid Interface Sci. 246 (2017) 133–152. https://doi.org/10.1016/j.cis.2017.05.018.

[8] L.B. Boinovich, E.B. Modin, A.R. Sayfutdinova, K.A. Emelyanenko, A.L. Vasiliev, A.M. Emelyanenko, Combination of Functional Nanoengineering and Nanosecond Laser Texturing for Design of Superhydrophobic Aluminum Alloy with Exceptional Mechanical and Chemical Properties, A.C.S. Nano. 11 (2017) 10113–10123. https://doi.org/10.1021/acsnano.7b04634.

[9] A. He, W. Liu, W. Xue, H. Yang, Y. Cao, Nanosecond laser ablated copper superhydrophobic surface with tunable ultrahigh adhesion and its renewability with low temperature annealing, Appl. Surf. Sci. 434 (2018) 120–125. https://doi.org/10.1016/j.apsusc.2017.10.143.

[10] R. Jagdheesh, J.J. Garc á-Ballesteros, J.L. Oca ña, One-step fabrication of near superhydrophobic aluminum surface by nanosecond laser ablation, Appl. Surf. Sci. 374 (2016) 2–11. https://doi.org/10.1016/j.apsusc.2015.06.104.

[11] R. Pan, H. Zhang, M. Zhong, Triple-Scale Superhydrophobic Surface with Excellent Anti-Icing and Icephobic Performance via Ultrafast Laser Hybrid Fabrication, A.C.S. Appl. Mater. Interfaces. 13 (2021) 1743–1753. https://doi.org/10.1021/acsami.0c16259.

[12] J. Han, M. Cai, Y. Lin, W. Liu, X. Luo, H. Zhang, K. Wang, M. Zhong, Comprehensively durable superhydrophobic metallic hierarchical surfaces Via tunable micro-cone design to protect functional nanostructures, R.S.C. Adv. 8 (2018) 6733–6744. https://doi.org/10.1039/c7ra13496g.

[13] S. Vignieri, “Green” revolution not so great for pollinators, Science (80-.). 346 (2014) 1338–1338. https://doi.org/10.1126/science.346.6215.1338-a.

[14] H. Gao, Y. Hu, Y. Xuan, J. Li, Y. Yang, R. V. Martinez, C. Li, J. Luo, M. Qi, G.J. Cheng, Large-scale nanoshaping of ultrasmooth 3D crystalline metallic structures, Science (80-.). 346 (2014) 1352–1356. https://doi.org/10.1126/science.1260139.

[15] S. Jin, Y. Wang, M. Motlag, S. Gao, J. Xu, Q. Nian, W. Wu, G.J. Cheng, Large-Area Direct Laser-Shock Imprinting of a 3D Biomimic Hierarchical Metal Surface for Triboelectric Nanogenerators, Adv. Mater. 30 (2018) 1–9. https://doi.org/10.1002/adma.201705840.

[16] A. Matsuda, T. Hongo, H. Nagao, Y. Igarashi, K.G. Nakamura, K. ichi Kondo, Materials dynamics under nanosecond pulsed pressure loading, Sci. Technol. Adv. Mater. 5 (2004) 511–516. https://doi.org/10.1016/j.stam.2004.01.016.

[17] G. Lu, D.W. Sokol, Y. Zhang, J.L. Dulaney, Nanosecond pulsed laser-generated stress effect inducing macro-micro-nano structures and surface topography evolution, Appl. Mater. Today. 15 (2019) 171–184. https://doi.org/10.1016/j.apmt.2019.01.005.

[18] K. Lu, J. Lu, Nanostructured surface layer on metallic materials induced by surface mechanical attrition treatment, Mater. Sci. Eng. A. 375–377 (2004) 38–45. https://doi.org/10.1016/j.msea.2003.10.261.

[19] N. Copper, T.H. Fang, W.L. Li, N.R. Tao, K. Lu, Tensile Plasticity in Gradient, Science (80-.). 331 (2011) 1587–1590.

[20] N.P. Kryuchkov, S.O. Yurchenko, Y.D. Fomin, E.N. Tsiok, V.N. Ryzhov, Complex crystalline structures in a two-dimensional core-softened system, Soft Matter. 14 (2018) 2152–2162. https://doi.org/10.1039/c7sm02429k.

[21] K.W. Jacobsen, J.K. Norskov, M.J. Puska, Interatomic interactions in the effective-medium theory, Phys. Rev. B. 35 (1987) 7423–7442. https://doi.org/10.1103/PhysRevB.35.7423.

[22] A. Stukowski, Structure identification methods for atomistic simulations of crystalline materials, Model. Simul. Mater. Sci. Eng. 20 (2012). https://doi.org/10.1088/0965-0393/20/4/045021.

[23] J. Long, Z. Cao, C. Lin, C. Zhou, Z. He, X. Xie, Formation mechanism of hierarchical Micro- and nanostructures on copper induced by low-cost nanosecond lasers, Appl. Surf. Sci. 464 (2019) 412–421. https://doi.org/10.1016/j.apsusc.2018.09.055.

[24] S. Agarwal, Engineering Chemistry, Eng. Chem. (2015) 988–994. https://doi.org/10.1017/cbo9781316146743.

[25] B.D. Cassie, Of porous surfaces, (1944) 546–551.

[26] Z.C. Cordero, B.E. Knight, C.A. Schuh, Six decades of the Hall–Petch effect – a survey of grain-size strengthening studies on pure metals, Int. Mater. Rev. 61 (2016) 495–512. https://doi.org/10.1080/09506608.2016.1191808.

[27] X.C. Liu, H.W. Zhang, K. Lu, Strain-induced ultrahard and ultrastable nanolaminated structure in nickel, Science (80-.). 342 (2013) 337–340. https://doi.org/10.1126/science.1242578.

[28] L. Yang, N.R. Tao, K. Lu, L. Lu, Enhanced fatigue resistance of Cu with a gradient nanograined surface layer, Scr. Mater. 68 (2013) 801–804.

https://doi.org/10.1016/j.scriptamat.2013.01.031.

[29] J.P. Chu, J.M. Rigsbee, G. Banaś, F. V. Lawrence, H.E. Elsayed-Ali, Effects of laser-shock processing on the microstructure and surface mechanical properties of hadfield manganese steel, Metall. Mater. Trans. A. 26 (1995) 1507–1517. https://doi.org/10.1007/BF02647602.

[30] T.Y. Tsui, W.C. Oliver, G.M. Pharr, Influences of stress on the measurement of mechanical properties using nanoindentation: Part I. Experimental studies in an aluminum alloy, J. Mater. Res. 11 (1996) 752–759. https://doi.org/10.1557/JMR.1996.0091.

[31] P. Fu, R. Chu, Z. Xu, G. Ding, C. Jiang, Relation of hardness with FWHM and residual stress of GCr15 steel after shot peening, Appl. Surf. Sci. 431 (2018) 165–169. https://doi.org/10.1016/j.apsusc.2017.09.136.

[32] A. V. Filippov, S.Y. Tarasov, S. V. Fortuna, O.A. Podgornykh, N.N. Shamarin, A. V. Vorontsov, Wear, vibration and acoustic emission characterization of sliding friction processes of coarse-grained and ultrafine-grained copper, Wear. 424–425 (2019) 78–88. https://doi.org/10.1016/j.wear.2019.02.014.

[33] X. Chen, Z. Han, K. Lu, Friction and Wear Reduction in Copper with a Gradient Nano-grained Surface Layer, A.C.S. Appl. Mater. Interfaces. 10 (2018) 13829–13838. https://doi.org/10.1021/acsami.8b01205.

[34] X. Liu, K. Wu, G. Wu, Y. Gao, L. Zhu, Y. Lu, J. Lu, High strength and high ductility copper obtained by topologically controlled planar heterogeneous structures, Scr. Mater. 124 (2016) 103–107. https://doi.org/10.1016/j.scriptamat.2016.07.003.

[35] Y. Wang, F. Guo, Q. He, L. Song, M. Wang, A. Huang, Y. Li, C. Huang, Synergetic deformation-induced extraordinary softening and hardening in gradient copper, Mater. Sci. Eng. A. 752 (2019) 217–222. https://doi.org/10.1016/j.msea.2019.03.020.

[36] R. Xiao, X.X. Li, L.H. Lang, Y.K. Chen, Y.F. Yang, Biaxial tensile testing of cruciform slim superalloy at elevated temperatures, Mater. Des. 94 (2016) 286–294. https://doi.org/10.1016/j.matdes.2016.01.045.

[37] J. Fan, L. Zhu, J. Lu, T. Fu, A. Chen, Theory of designing the gradient microstructured metals for overcoming strength-ductility trade-off, Scr. Mater. 184 (2020) 41–45. https://doi.org/10.1016/j.scriptamat.2020.03.045.

[38] L. Zhu, X. Guo, J. Lu, Surface stress effects on the yield strength in nanotwinned polycrystal face-centered-cubic metallic nanowires, J. Appl. Mech. Trans. ASME. 81 (2014) 1–7. https://doi.org/10.1115/1.4028039.